Crystal and molecular structure of V-amylose complexed with butan-1-ol

Cong Anh Khanh Le, Karim Mazeau, Yoshiharu Nishiyama, Yu Ogawa, Luc Choisnard, Denis Wouessidjewe, Jean-Luc Putaux

Crystal and molecular structure of V-amylose complexed with butan-1-ol

Cong Anh Khanh Le[a], Karim Mazeau[a], Yoshiharu Nishiyama[a], Yu Ogawa[a], Luc Choisnard[b], Denis Wouessidjewe[b], and Jean-Luc Putaux[a,*]

[a] *Univ. Grenoble Alpes, CNRS, CERMAV, F-38000 Grenoble, France*

[b] *Univ. Grenoble Alpes, CNRS, DPM, F-38000 Grenoble, France*

* corresponding author - email: jean-luc.putaux@cermav.cnrs.fr

Published in: **Polymer** *243* (2022), 124651

DOI: 10.1016/j.polymer.2022.124651

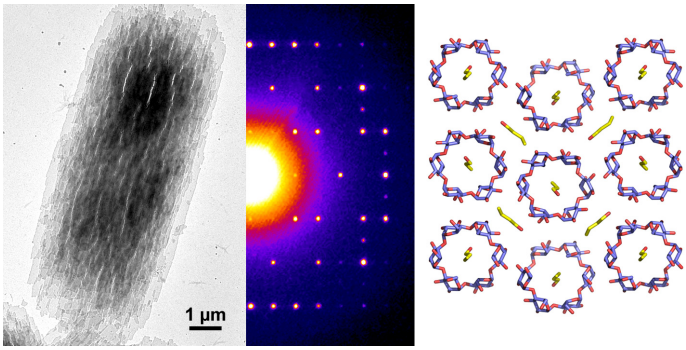

Abstract

Chain-folded lamellar V-amylose single crystals were prepared by adding butan-1-ol to hot dilute aqueous solutions of native amylose. The base-plane electron and X-ray diffraction patterns recorded from hydrated specimens agreed with a $P2_12_12_1$ space group and an orthorhombic unit cell. A molecular model resulting from an exhaustive search of helix position and restrained structure refinement against diffraction data was proposed. The unit cell contains 4 antiparallel left-handed 6-fold amylose single helices with 1 butan-1-ol molecule located inside each of the helical cavities. In addition, 4 butan-1-ol and 20 water molecules are distributed in the 4 interstitial spaces. The amylose helices form rows along the *b*-axis that are alternatively shifted by ±*b*/8 with respect to one another, which validates the geometrical model proposed by Helbert and Chanzy in 1994.

Keywords: V-amylose, butan-1-ol, inclusion compounds, structure refinement

1. Introduction

While he was studying the cooking and aging of bread, in 1930, Katz described a powder X-ray diffraction (XRD) pattern that was different from the known A- and B-type patterns from native starch granules. He named this new crystalline form "V" after the German word "Verkleisterung" that means gelatinization [1]. V-type patterns were also observed when starch pastes were precipitated with some alcohols [2] and Bear identified different V-type signatures depending on the precipitating agent [3]. Meyer et al. had fractionated native starch into two components (namely, the mostly linear amylose and the branched amylopectin) in hot water [4]. However, Schoch [5] and Kerr et al. [6,7] described a more efficient separation route based on the selective precipitation of amylose with *n*-butanol (referred to as butan-1-ol in the present article). This method was studied and refined by many authors during the following decades [8-12].

Rundle and Edwards characterized by XRD wet (*i.e.*, in water saturated with butan-1-ol), partially hydrated (V_h) and anhydrous (V_a) samples prepared from $V_{butan\text{-}1\text{-}ol}$ crystalline powders [13]. In the first two cases, the authors proposed that 6-fold amylose single helices with a diameter of 1.37 nm and a helical repeat of 0.8 nm were closely packed into orthorhombic unit cells. In the wet complex, butan-1-ol molecules were located inside the helical cavity. The unit cell of V_a crystals was hexagonal with a helix diameter of 1.30 nm [13]. Comparing the powder XRD patterns of V-type complexes prepared with methanol, ethanol and propan-1-ol, Valletta et al. discussed the origin of the two types of 6-fold helices [14]. Later on, the $V_{butan\text{-}1\text{-}ol}$ [15], V_h [16] and V_a [17] structures were described in more details using higher resolution XRD data collected from oriented fibers.

Kerr and Severson recorded optical micrographs of $V_{butan\text{-}1\text{-}ol}$ crystals with a rectangular platelet shape [7]. However, the contribution of transmission electron microscopy (TEM) and electron diffraction (ED) was particularly significant to study the morphology and structure of $V_{butan\text{-}1\text{-}ol}$ single crystals. In 1963-64, Hirai et al. [18], Yamashita [19] and Manley [20] published the first TEM images and ED patterns of 8-10 nm-thick lamellar $V_{butan\text{-}1\text{-}ol}$ single crystals, prepared from dilute aqueous amylose solutions. The authors determined that the helices were oriented perpendicular to the lamellar plane and, considering the crystal thickness and average degree of polymerization (DP) of amylose, that the chains were folded, like in single crystals of flexible linear synthetic polymers. Similar TEM images of $V_{butan\text{-}1\text{-}ol}$ lamellar crystals were later published by Bittiger and Husemann [21], Yamashita [22] and Yamashita et al. [23].

One of the main difficulties to characterize the structure of $V_{butan\text{-}1\text{-}ol}$ complexes was the loss of volatile guest molecules under the vacuum of the electron microscope. A typical paradox was that, at room temperature, hexagonal electron diffraction patterns were recorded from rectangular crystals [22]. Booy et al. made a major progress by probing solvated $V_{butan\text{-}1\text{-}ol}$ lamellar crystals that had been quench-frozen in liquid nitrogen prior to the introduction in the microscope and kept at low temperature during the low-dose observation [24]. The ED patterns unambiguously suggested an

orthorhombic unit cell with the *a*-parameter twice as large as that proposed by Rundle and Edwards [13] and Hinkle and Zobel [15] from XRD data. The helical repeat of about 0.8 nm was confirmed, *i.e.*, equal to that of 6-fold V_h complexes [16]. Once the crystals were warmed up and dried in the microscope, their structure was converted to the close-packed hexagonal V_h structure observed by Yamashita [19] and Manley [20], supposedly due to the loss of included butan-1-ol molecules.

By analyzing series of ED patterns recorded from tilted solvated $V_{butan\text{-}1\text{-}ol}$ and $V_{pentan\text{-}1\text{-}ol}$ crystals, Helbert and Chanzy confirmed the orthorhombic $P2_12_12_1$ symmetry and proposed a model where the guest molecules were located both inside and between the 6-fold helices [25]. In addition, the conversion to the V_h structure upon desolvation without morphological change supported the occurrence of 6-fold helices in the $V_{butan\text{-}1\text{-}ol}$ crystals. However, the model was purely geometrical and based on symmetry and morphological considerations, without considering the diffraction intensity data. The present work expands from that of Helbert and Chanzy by exploring the packing possibilities of amylose helices and guest distribution, comparing the diffraction intensities of the calculated models with the experimental data. We checked the robustness of the previously proposed model as well as the extent of the molecular information that could be extracted experimentally. Considering the important role of butan-1-ol in the selective fractionation of starch [26-34] and the early studies of crystalline V-type inclusion compounds [13-23,35], solving the crystal structure of the $V_{butan\text{-}1\text{-}ol}$ complex appeared to have a particular historical significance.

2. Experimental Section

2.1. Preparation of the crystalline complexes

Native potato amylose and butan-1-ol were purchased from Sigma-Aldrich. The amylose was further purified [36] and its weight-average degree of polymerization ($\overline{DP_w}$) was 2500 [37]. Amylose (10 mg) was dispersed in ultrapure water (10 mL). The suspension was submitted to nitrogen bubbling for 20 min, autoclaved for 30 min at 160 °C, cooled down to 90 °C and poured into a glass tube containing 1 mL butan-1-ol preheated at 90 °C. The tube was incubated at 40 °C for 3 days, then cooled down to room temperature. The solid residue was recovered by slow centrifugation, washed three times with water saturated with butan-1-ol and kept in this aqueous medium at room temperature for further analysis.

2.2. X-ray diffraction (XRD)

After crystallization, the sedimented fraction was centrifuged for 10 min at 12000 *g*. The wet pellet was deposited onto absorbent paper to remove the excess liquid and conditioned at 95 % relative humidity (r.h.). Strips of the resulting hydrated mat were rapidly introduced into glass capillaries that were flame-sealed and X-rayed in vacuum using a Philips PW3830 generator operating at 30 kV and 20 mA (Ni-filtered CuKα radiation, λ = 0.1542 nm). Two-dimensional diffraction patterns were recorded on Fujifilm imaging plates, read off-line with a Fujifilm BAS

1800-II bioimaging analyzer. Diffraction profiles were calculated by rotational average of the powder patterns. The diffraction data were calibrated using a calcite powder standard and the unit cell parameters were refined with the CelRef module of the LMGP package [38].

2.3. Transmission electron microscopy (TEM) and electron diffraction (ED)

Droplets of dilute crystal suspensions were allowed to dry on glow-discharged carbon-coated grids. The specimens were observed under low dose illumination with a Philips CM200 'Cryo' microscope operating at 200 kV. For electron diffraction, just after drying of the excess liquid, the TEM grids were rapidly mounted on a Gatan 626 specimen holder and fast-frozen into liquid nitrogen. The holder was then introduced in the microscope and cooled down to a temperature of -177 °C. ED patterns were recorded at 200 kV from selected areas of about 1 μm^2 and calibrated using a gold-coated carbon film as standard. In the following, "base-plane ED patterns" will refer to patterns recorded along the [001] *c*-axis of the crystal structure, *i.e.*, perpendicular to the *(a,b)* plane of the lamellae and parallel to the axis of the amylose helices. Images were recorded on a TVIPS TemCam F216 camera and ED patterns on Fujifilm imaging plates. The intensity of the diffraction spots was measured using the procedure described elsewhere [39]. In view of the symmetry of the patterns, the intensities of *hk*0, -*hk*0, *h*-*k*0 and -*h*-*k*0 reflections were averaged.

2.4. Density measurement

Fragments of mats of crystals equilibrated at 95% r.h. were floated in 1,2-dichloroethane (d = 1250 g L^{-1}) to which 1,1,2-tricloro-1,2,2,-trifluoroethane (d = 1560 g L^{-1}) was slowly added. When the film remained in equilibrium in the mixture, the liquid density was assumed to match that of the film. The liquid density was measured using a pycnometer bottle.

2.5. ^{13}C CP/MAS nuclear magnetic resonance (NMR) spectroscopy

The hydrated sample pellets were packed into a zirconia rotor. Solid-state ^{13}C NMR analyses were performed on a Bruker Avance III 400 MHz spectrometer (^{13}C frequency of 100.6 MHz) using cross polarization (CP) and magic angle spinning (MAS). The spinning speed was set at 12 kHz, with a sweep width of 29761 Hz, and a recycle delay at 2 s. Each spectrum was averaged over 6000 scans. The ^{13}C chemical shifts were calibrated with the resonance of the glycine carboxyl group (176.03 ppm).

2.6. Structural analysis

2.6.1. Building amylose helices and search of favorable helix positions in the unit cell

Stereoregular left- and right-handed helices (L and R, respectively) having 6 and 7 residues per helical turn and a pitch of 0.80 nm were generated from an α-D-glucosyl residue in the $^4C_1$ chair shape as described elsewhere [39]. Amylose chains are constituted by a rather rigid backbone with flexible hydroxymethyl groups. The hydroxymethyl protruding from each pyranose

ring has three stable orientations: *gauche-gauche*, *gauche-trans* and *trans-gauche* (*gg*, *gt* and *tg*, respectively) (**Scheme S1**). Consequently 3^6 and 3^7 conformers are *a priori* accessible for 6- and 7-fold amylose helices, respectively. Therefore, to develop a procedure applicable to all amylose crystalline complexes and to make this conformational diversity manageable, the hydroxy groups on the C6 atoms were replaced by hydrogen atoms, thus screening out the steric hindrances. The helices, referred to as L6, R6, L7 and R7 in the following, were relaxed by energy-minimization using the Universal Force Field [40] in the Forcite module of Materials Studio [41]. Each helix was introduced into the unit cell with parameters and space group determined from the diffraction data.

The position and rotation of the helices in the unit cell were systematically explored. One helix was placed at the (0,0) starting position and the $P2_12_12_1$ space group (Supplementary Data **Fig. S1**) generated three symmetry-related helices. The helices were then translated along the *a* and *b* axes by 0.01 increments in fractional coordinate. In addition, at each (*x*,*y*) position, the helix was rotated about its axis in 1° steps between 0 and 360°, and, for each rotation angle, translated along the *c*-axis with a step of 0.04 in fractional coordinate. The packing energy, *i.e.*, the contact energy between the helices, was calculated for each structural microstate using a Buckingham potential with a cutoff of 1 nm. The values of the A, B and C constants for each pair of atom types were taken from Dauchez et al. [42]. For each (*x*,*y*) position, only the lowest energy model with respect to the rotation and *z*-translation was retained and the corresponding XRD powder profile and base-plane ED pattern were calculated with an in-house program using the Computational Crystallography ToolBox (CCTBX) library [43]. The calculated patterns were compared with the experimental data using reliability factors with the following generic expression:

$$R = 1 - \left(\frac{\boldsymbol{I}_{obs} \cdot \boldsymbol{I}_{cal}}{\|\boldsymbol{I}_{obs}\| \ \|\boldsymbol{I}_{cal}\|}\right)^2 \qquad (1)$$

where $\boldsymbol{I}_{obs}$ and $\boldsymbol{I}_{cal}$ are the sets of observed and calculated intensities represented as vectors. The agreement with the X-ray profile (R_{XRD}) was calculated assuming a crystal size of $50 \times 50 \times 8$ nm^3 and an isotropic orientation distribution of the crystals. In this case, the vector $\boldsymbol{I}$ corresponds to the intensities of the powder diffraction profile at different angles, which are sum of contributions from overlapping reflections [39]. The agreement with the base-plane ED pattern (R_{ED}) was also calculated using **Eq. 1** but here, the vectors were composed of the integrated intensity of each reflection.

Color surface maps in the *(a,b)* base plane corresponding to the potential energy and the R_{XRD} and R_{ED} reliability factors were drawn using Gnuplot [44] and the molecular models corresponding to the minima in each map were built. Proper amylose chains were completed by replacing one selected hydrogen atom of the C6-methyl group of each residue by a hydroxy group with the *gg* orientation. Then, butan-1-ol and water molecules were added in the free volumes of the unit cells. The complete systems were energy-optimized using the Universal Force Field [40]. The optimization was carried out in two steps. At first, the atomic coordinates of the amylose helix

were constrained and only the butan-1-ol and the water molecules were allowed to move. This step allowed finding favorable positions of the guest molecules while maintaining the position, orientation and conformation of the amylose chains. In the second step, all atoms in the cell were free to move. All molecular models have been drawn using Materials Studio [41] and Mercury [45].

2.6.2. Model refinement

The structures were refined against experimental ED data using the SHELXL program [46]. The atomic scattering factors for electrons were taken from the International Tables for Crystallography [47]. The models were refined using the conjugate-gradient least-square (CGLS) regression method with isotropic thermal parameters. The chemically-bound first and second neighbor atoms were restrained using the DFIX and DANG instructions in SHELXL. Anti-bumping restraints were applied to avoid collision. At the beginning of the refinement, the standard deviation *sd* for 1-2 and 1-3 distances was set at 0.002 in the first DEFS parameter, *i.e.*, 10 times lower than the default value (0.02) to maintain reasonable values of the internal geometry of amylose. In the final refinement, *sd* was then increased to 0.01 and finally to 0.02 to allow the helix to further relax.

ED patterns were calculated by convoluting the calculated intensities with a 2D Gaussian function. The similarity with the experimental data was evaluated via the classical R_1-factor:

$$R_1 = \frac{\sum||F_{obs}|-|F_{cal}||}{\sum|F_{obs}|} \qquad (2)$$

where F_{obs} and F_{cal} are the observed and calculated structure factors, respectively. XRD profiles were calculated from the molecular models using Mercury [45]. The fit with the experimental profile was optimized by adjusting the full width at half-maximum (FWHM) of the peaks and specifying a preferred orientation of the crystals through the March-Dollase parameter [48]. The agreement with the experimental data (R_{XRD}) was then calculated using **Eq. 1**.

3. Results and Discussion

3.1. Crystal morphology and unit cell

Fig. 1 shows electron micrographs of typical crystals of $V_{butan\text{-}1\text{-}ol}$ prepared from dilute aqueous amylose solutions. They generally consist of stacks of thin rectangular lamellae (**Fig. 1a**). Each lamella is about 2-5 µm wide and 8-12 µm long. The crystals seem to have thickened by homoepitaxial growth, maintaining a common longitudinal orientation. In addition, cross-shaped or rosette-shaped twins consisting of two or three crystals misoriented by about 60 or 90° with respect to each other were usually observed (**Fig. 1b** and **1c**). As mentioned in previous studies, longitudinal cracks frequently occurred along the rectangular lamellae [20,22,24,25]. They were caused by an anisotropic shrinkage of the unit cell upon drying of the crystals in air or under vacuum in the TEM, while the supporting carbon film is stable. These cracks were absent when the crystals were observed under frozen-solvated conditions.

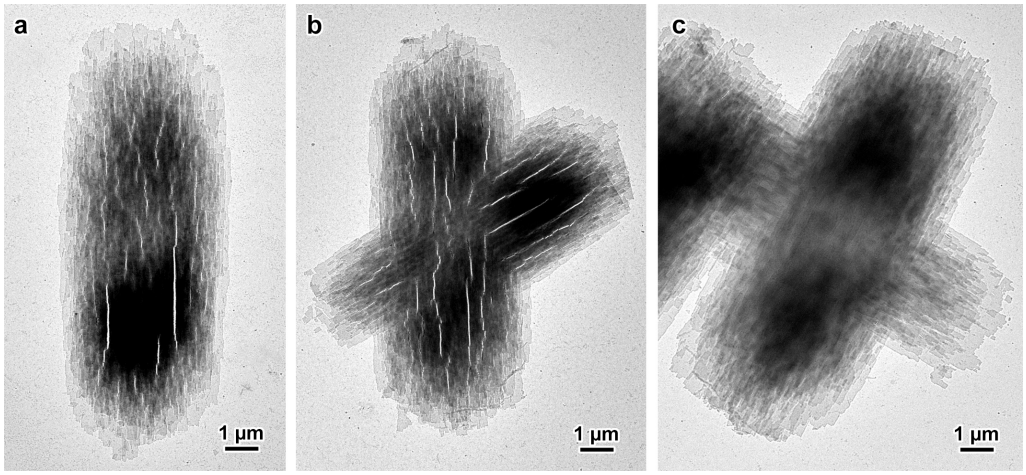

Figure 1. TEM images of crystals of V-amylose complexed with butan-1-ol: a) single crystal; b) 60°-twinned crystals; c) 90°-twinned crystals.

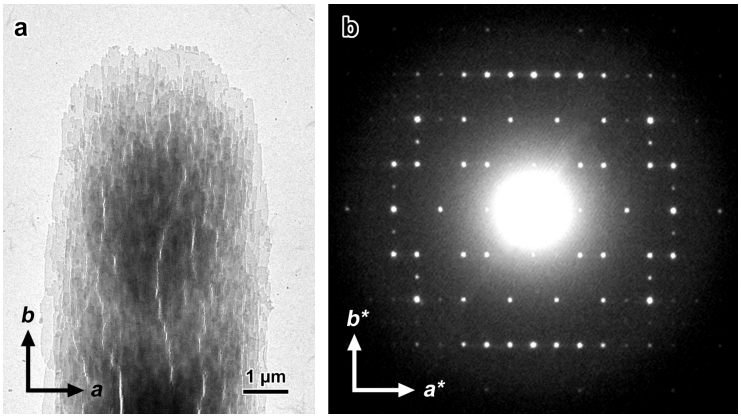

Figure 2. a) TEM image of a dry lamellar crystal of V-amylose complexed with butan-1-ol; b) base-plane electron diffraction pattern recorded at low temperature from a frozen-solvated $V_{butan\text{-}1\text{-}ol}$ single crystal.

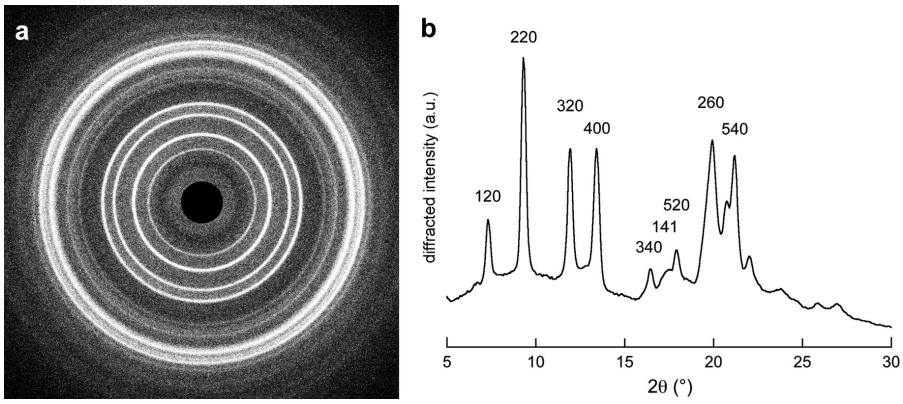

Figure 3. a) XRD pattern of V-amylose complexed with butan-1-ol; b) corresponding diffraction profile with indexes of the main peaks.

Fig. 2b shows a typical base-plane ED pattern recorded at low temperature from one frozen-solvated $V_{butan\text{-}1\text{-}ol}$ crystal. The pattern is unique, which means that all the constituting unit lamellae are crystallographically aligned into one crystal. The pattern is properly oriented with respect to the crystal shown in **Fig. 2a** and the *b*-axis of the unit cell is aligned along the long axis of the crystal. The diffraction spots extend to a resolution of 0.24 nm and are symmetrically distributed in a lattice defined by the two orthogonal axes *a** and *b** aligned parallel to the shorter and longer dimensions of the lamella, respectively. This pattern is identical to those reported by Booy et al. [24] and Helbert and Chanzy [25]. It can be indexed according to a rectangular two-dimensional unit cell with lattice parameters *a* = 2.65 ± 0.01 nm, *b* = 2.74 ± 0.01 nm. The XRD profile is similar to that published by Le Bail et al. [49] and, assuming an orthorhombic unit cell, the refined parameters are: *a* = 2.655 ± 0.001 nm, *b* = 2.708 ± 0.001 nm, and *c* = 0.798 ± 0.001 nm (**Fig. 3** and Supplementary Data **Table S1**), in agreement with the values reported in previous studies [24,25]. However, for consistency with other known V-amylose allomorphs and following the convention proposed by Donnay [50], *i.e. a* < b, we have switched the *a* and *b* values with respect to those given in the previous studies. A list of independent intensities for reflections up to a resolution 0.24 nm, averaged from several ED patterns, is presented in **Table S2.**

3.2. ^{13}C CP/MAS NMR spectroscopy

Fig. 4a shows a typical ^{13}C CP/MAS NMR spectrum recorded on hydrated crystals of $V_{butan\text{-}1\text{-}ol}$. The resolved resonances at 102.4, 81.8, 74.9, 71.7 and 61.0 ppm can be assigned to the C1, C4, C3, and C2-C5 and C6 carbon atoms of the glucosyl units, respectively. One small peak and a shoulder at 100.4 and 99.5 ppm, respectively, indicate the presence of a small amount of B-amylose (**Fig. 4b**) likely due to the crystallization of uncomplexed amylose [51,52]. The broad peak at 58-63 ppm, that can be deconvoluted into three contributions at about 59.6, 61 and 62 ppm, is an overlap of the resonance of carbon C6 of the glucosyl units and that of carbon C(OH) of butan-1-ol (**Fig. 4c**). The sharp peaks at 34.9, 19.4 and 14.3 ppm correspond to the resonances of other carbon atoms of butan-1-ol [53,54].

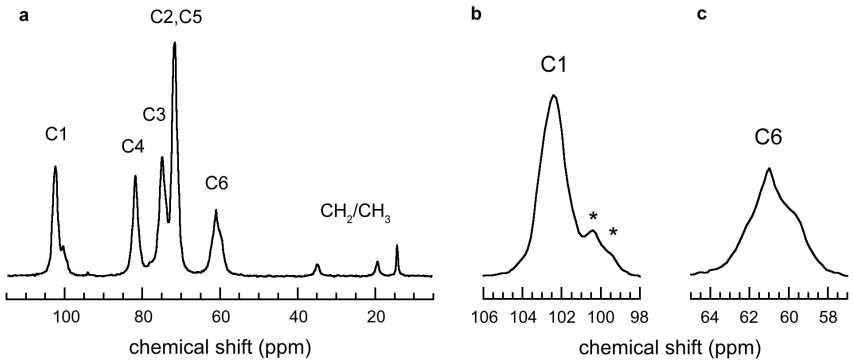

Figure 4. a) ^{13}C CP/MAS spectrum of V-amylose complexed with butan-1-ol. The contributions of carbons C1 (b) and C6 (c) from glucosyl units have been enlarged. The resonances indicated by * correspond to a fraction of residual B allomorph.

The chemical shifts of the C1 and C4 atoms depend on the torsion angles about the glucosidic linkages and thus reflect the global helical conformation of the chain [51,52,55]. Gidley and Bociek reported a 1 ppm upfield shift of C1 and C4 for 8-fold helices compared to 6- and 7-fold helices but did not distinguish between the latter two [55]. Kawada and Marchessault [53] also observed that the complexes prepared with dodecanoic acid, which would contain 6-fold helices, presented the same C1 chemical shift at 103 ppm as 7-fold V_{thymol} [56]. However, more recent studies identified two different C1 resonance domains: 102.2–102.7 for V6 structures and 103.3–103.4 for V7 [49,57,58]. In the present study, the C1 peak in $V_{butan\text{-}1\text{-}ol}$ was found at 102.4 ppm which suggests that the complex contains 6-fold helices.

In carbohydrates, the C6 resonance is sensitive to the orientation of the hydroxymethyl group. Three groups of correlations have been identified for some model monosaccharides: 60.0–62.6 ppm for *gg*, 62.5–64.5 ppm for *gt*, and 65.5–66.5 ppm for *tg* [59]. In cyclodextrins, the chemical shifts in the 59.6–61.7 ppm and 62.7–65.9 ppm regions are related to *gg* and *gt* conformations, respectively [60]. In the case of $V_{butan\text{-}1\text{-}ol}$ complexes, the rather broad peaks of the C6 carbons of amylose is centered around *ca.* 61 ppm (**Fig. 4**), in agreement with previous studies [49,53], which suggests that the main orientation of the hydroxymethyl group is *gg*.

3.3. Molecular modeling and crystal structure determination

3.3.1. Selection of the helix conformation and search for the helix position in the unit cell

Since V-type complexes prepared in the presence of propan-2-ol [39], ibuprofen [58], some fatty acids [36] and diols [37] have been shown to contain 7-fold amylose helices, the possibility that $V_{butan\text{-}1\text{-}ol}$ crystals also contained 7-fold helices was not ruled out *a priori*, in order to assess the selectivity of our packing analysis approach. The 4 constructed single helices, namely L6, R6, L7 and R7, with omitted O6H hydroxy groups, are shown in **Fig. 5**. Each helix was introduced in the orthorhombic unit cell with parameters determined from the crystallography data, and the symmetry operators of the $P2_12_12_1$ space group generated three copies. For simplicity, in the following, *x* and *y* being the fractional coordinates of the helix, the selected models will be identified by L6/L7_nnpp or R6/R7_nnpp, nn and pp being 100 × *x* and 100 × *y*, respectively, ranging from 0 to 99.

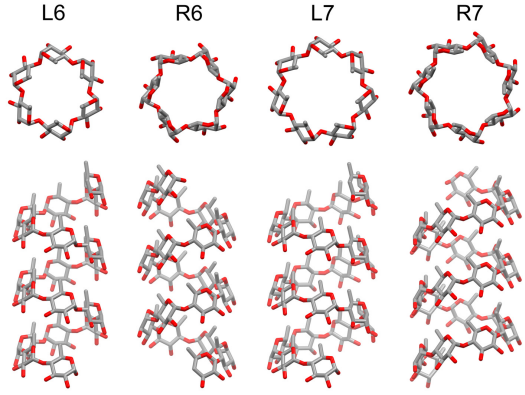

Figure 5. Axial (top) and longitudinal (bottom) views of stereoregular 6- and 7-fold left- and right-handed helices (L and R, respectively) without O6H hydroxy groups. Hydrogen atoms have been omitted for clarity.

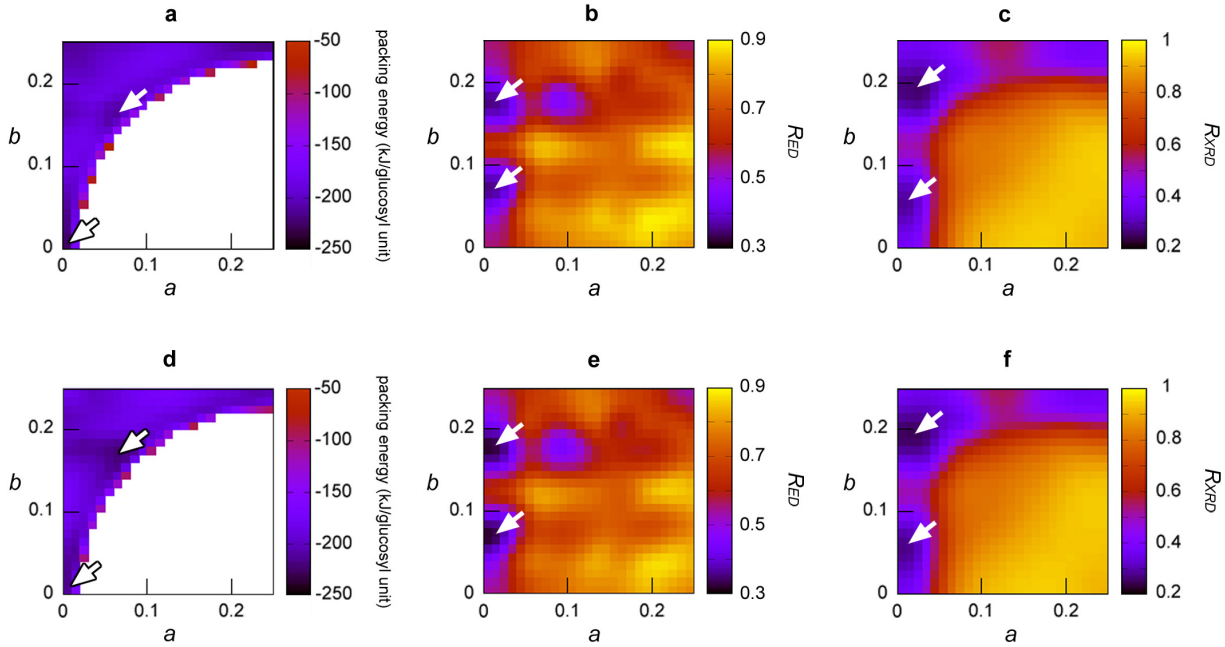

Figure 6. a,d) Color maps of the packing energy of models based on left- (a) and right-handed (b) 6-fold amylose helices (L6 and R6, respectively) without O6H hydroxy groups. The helices were systematically translated and rotated in the (*a,b*) plane of the unit cell. b,e) R_{ED}-factor between the observed and calculated ED diagrams for L6 (b) and R6 (e) helices; c,f) R_{XRD}-factor between the observed and calculated XRD profiles for L6 (c) and R6 (f) helices. The helix position in the unit cell is indicated with fractional coordinates. Considering the symmetry of the $P2_12_12_1$ space group, only 1/16th of the *(a,b)* plane was displayed ($0 \le x \le 0.24$, $0 \le y \le 0.24$). In all maps, the minima are indicated by arrows. Both *R*-factors were calculated using **Eq. 1**.

Table 1. Helix position, packing energy, R_{ED} and R_{XRD} factors of selected models based on left- and right-handed 6-fold amylose single helices (L6 and R6), within 1/16th of the unit cell (see color maps in **Fig. 6**). The selected models correspond to a local minimum in either one of the three maps.

Model name	Position of the helix center (fractional coordinates)		Packing energy (kJ/glucosyl unit)	R_{ED}	R_{XRD}
	x	*y*			
L6_0000	0.00	0.00	-233.2	0.55	0.37
L6_0007	0.00	0.07	-203.4	0.35	0.28
L6_0118	0.01	0.18	-197.1	0.35	0.28
L6_0617	0.06	0.17	-212.5	0.57	0.50
R6_0000	0.00	0.00	-226.2	0.54	0.37
R6_0007	0.00	0.07	-194.7	0.31	0.28
R6_0118	0.01	0.18	-211.2	0.31	0.27
R6_0718	0.07	0.18	-223.9	0.53	0.50

The energy and diffraction agreement-maps corresponding to the L6 and R6 helices are shown in **Fig. 6**, while the maps for L7 and R7 are given in Supplementary Data **Fig. S2**. Considering the symmetry of the $P2_12_12_1$ space group (Supplementary Data **Fig. S1**), only $1/16^{th}$ of the *(a,b)* plane was displayed ($0 \leq nn \leq 24$, $0 \leq pp \leq 24$). The models based on 6-fold helices were the most energetically favored while the packing energy of structures based on 7-fold helices was significantly higher. Supplementary Data **Fig. S3** shows models corresponding to the packing energy minima in the maps of L6, R6, L7 and R7 helices, projected on the (*a*,*b*) plane of the unit cell. While the models based on 6-fold helices seemed acceptable in terms of packing, significant interhelix collisions were observed in the models containing 7-fold helices, which explains the globally higher packing energies. Consequently, the structures involving 7-fold helices were discarded for further calculations.

Structures based on L6 and R6 helices have similar packing energy profiles (**Fig. 6a** and **6d**, respectively) although, for a given position in the map, the packing energy of the R6 model is slightly lower than its L6 counterpart (**Table 1**). In both cases, the map contains a fairly extended region within which the packing energy does not vary much. Indeed, as seen in Supplementary Data **Fig. S3**, the unit cell dimensions offer to 6-fold helices a large accessible volume to explore without generating significant contacts and energy penalties. It must be noted that the energy calculation only considered Buckingham's non-bonded interactions between amylose chains lacking O6H hydroxy groups, and no electrostatic interactions were considered. The rationale for this is that in polysaccharide systems, the dispersion interaction would still dominate the cohesion, especially in the presence of water, and the steric repulsion is the most important factor to consider. For a given helix distribution, the R_{ED}-factor is also slightly lower for R6 models than for L6 ones (**Table 1**). The R_{XRD}-factors are rather similar for the two types of helices. At this stage, we cannot choose between L6 and R6 models.

The positions of the minima in R_{ED} and R_{XRD} maps are fairly close, but they are different from those of the minima in the packing energy maps (**Figs. 6** and **S2**). We selected models corresponding to minima in either packing energy or *R*-factor maps for further calculation. Eight models, namely L6_0000, L6_0007, L6_0118, L6_0617 (**Fig. 7**), R6_0000, R6_0007, R6_0118 and R6_0718 (Supplementary Data **Fig. S4**), were selected as starting models for structure refinement. Their corresponding packing energy and *R*-factors are summarized in **Table 1**.

In L6_0000 and R6_0000 models, the helices are arranged in rows parallel to the *a* and *b* axes. For L6_0007, R6_0007, L6_0118 and R6_0118, the helices are aligned along the *b*-axis and form rows alternately shifted by $-\pm b/8$ with respect to one another. However, the positions of the helices within the unit cell and with respect to the symmetry axes (Supplementary Data **Fig. S1**) are different in L6_0007 / R6_0007 and L6_0118 / R6_0118. In these 4 models, the helices are not close-packed and both intra- and interhelical spaces are large enough to host butan-1-ol molecules. The helix distribution in L6_0617 and R6_0718 can be described as a mixture of two

motifs of arrangement of 4 helices. In one motif, the helices are close-packed while in the other, they are organized into a nearly tetragonal fashion, with an interhelical space in which butan-1-ol molecules can be hosted. Such a helix pattern has recently been proposed to describe the drying mechanism of V-type complexes with hexane-1,6-diol, although this structure has never been identified by direct crystallization of amylose [37].

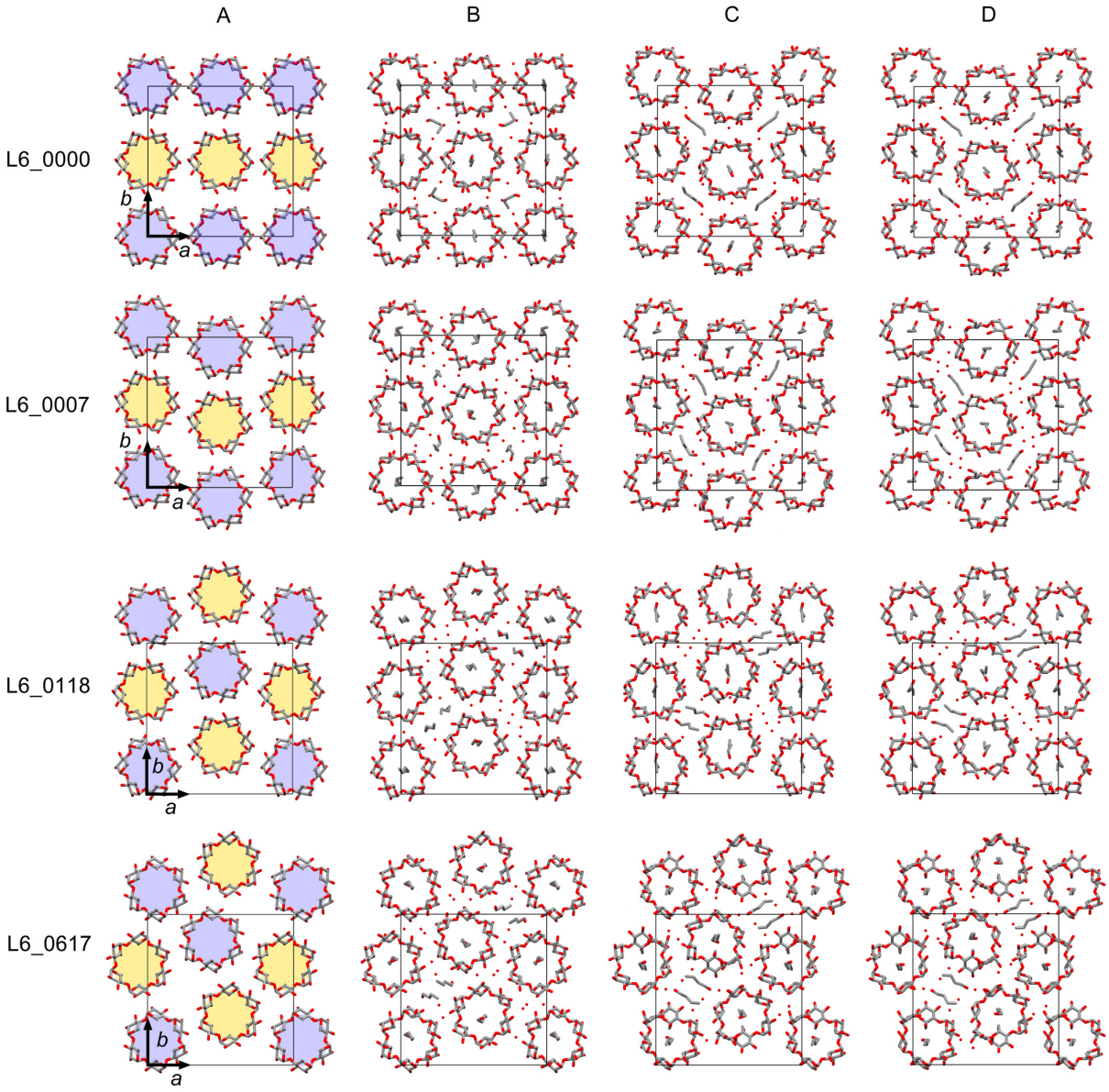

Figure 7. Column A: projections on the *(a,b)* plane of the L6 models corresponding to minima in the maps of **Fig. 6** (**Table 1**). The helices are stereoregular and without O6H hydroxy groups. The blue and yellow colors distinguish between up and down helices organized in an antiparallel fashion. Column B: Hydroxymethyl groups in *gg* conformation were added as well as butan-1-ol (*trans* conformation) and water molecules. The models were minimized in Materials Studio then used as input files in SHELXL. Column C: models refined against ED data in SHELXL with the hydroxymethyl conformation constrained to *gg* and butan-1-ol in *trans* conformation; column D: refined models with unrestrained hydroxymethyl conformation. In all models, the hydrogen atoms have been omitted for clarity and the unit cells are indicated.

3.3.2. Addition of the O6H hydroxy group and guest molecules

The O6H hydroxy group with a *gg* orientation was added to each glucosyl residue of the helix. For simplicity, the carbon chain of all butan-1-ol guests was in the *trans* conformation similar to that adopted by the molecule in the crystalline state [61]. This conformation corresponds to the global minimum of the internal energy predicted by quantum mechanics [62]. The stoichiometry of butan-1-ol and water molecules was estimated from the experimental crystal density of 1.38 ± 0.02 $g.cm^{-3}$, in agreement with the value reported by Helbert and Chanzy [25]. We considered the volume of the unit cell and the mass of the 4 portions of 6-fold amylose chains. Helbert and Chanzy previously estimated that the interhelical space in each unit cell would contain 4 butan-1-ol molecules, along with some water molecules [25]. Assuming that 1 butan-1-ol is located in each of the 4 amylose helices, and 1 butan-1-ol in each of the 4 interhelical spaces, the unit cell would thus contain a total of 8 butan-1-ol and 20 interstitial water molecules.

After addition of the O6H hydroxy group, butan-1-ol and water molecules, the geometry of the selected models was optimized, as detailed in the Experimental Section: optimization of guest molecules with frozen helices, followed by the optimization of all atoms. The L6_0000, L6_0007, L6_0118 and L6_0617 packing models of rigid helices are shown in **Fig. 7** (column A) as well as the corresponding geometry-optimized models after addition of the O6H hydroxy group, butan-1-ol and water molecules (column B). After the geometry optimization, the helices have lost the stereoregular hexagonal symmetry.

3.3.3. Structure refinement

The four geometry-optimized structures were used as input for SHELXL refinement against ED data. This refinement was carried out in two steps. In the first one, the orientation of the hydroxymethyl groups of the amylose chains together with the conformation of the butan-1-ol alkyl moiety were constrained to maintain the *gg* and the *trans* conformation respectively. In the second step, the constraint on the hydroxymethyl groups was lifted and only that on butan-1-ol molecules was maintained. The refinement procedure allowed finding the atomic arrangements that increased the match between observed and calculated intensities, indicated by a lower R_1-factor. Using the average ED intensities up to a resolution of 0.24 nm (71 independent diffraction spots, Supplementary Data **Table S2**) and the default value of the effective standard deviation (*sd* = 0.02 defined in the DEFS command of SHELXL) for restrained parameters, no model converged to the experimental diffraction intensities. R_1 was close to 1 and the helical conformation was lost. Therefore, in the first several refinement steps, *sd* was fixed at a value 10 times lower than the default one in order to preserve a reasonable internal geometry of the molecules (bond length and bond angles). The resolution of the ED data was first limited to 0.35 nm, then to 0.30 nm and finally to 0.24 nm. In the final refinement step, the default *sd* value was used to allow the helices to relax while the resolution remained limited to 0.24 nm.

Table 2. R_1-factor of selected models refined against electron diffraction data using SHELXL. *d* is the resolution of the used reflections. *sd* is the effective standard deviation for restrained distances between bonded atoms and bond angles, defined in the DEFS instruction in SHELXL. R_{XRD} was calculated considering a preferential orientation of the crystals along the *c*-axis (FWHM = 0.37 and March-Dollase parameter = 3) [48].

Starting model	R_1				R_{XRD}	
	d > 0.35 nm *sd* = 0.002 [a]	*d* > 0.24 nm *sd* = 0.002 [a]	*d* > 0.24 nm *sd* = 0.02 [a]	*d* > 0.24 nm *sd* = 0.02 [b]	*gg* constrained [a]	free [b]
L6_0000	0.58	0.30	0.21	0.18	0.16	0.16
L6_0007	0.31	0.41	0.23	0.15	0.27	0.19
L6_0118	0.30	0.39	0.25	0.19	0.32	0.19
L6_0617	0.81	0.75	0.57	0.55	0.63	0.59
R6_0000	0.81	0.71	0.34	0.30	0.28	0.29
R6_0007	0.49	0.44	0.36	0.32	0.27	0.26
R6_0118	0.51	0.58	0.32	0.28	0.34	0.22
R6_0718	0.87	0.78	0.67	0.55	0.62	0.60

[a] the hydroxymethyl group at C6 was constrained in *gg* conformation; the carbon chain of butan-1-ol was constrained in the *trans* conformation.

[b] the hydroxymethyl group at C6 was free to relax; the carbon chain of butan-1-ol was constrained in the *trans* conformation.

The refinement results are summarized in **Table 2** and the corresponding refined models are shown in **Fig. 7** (columns C and D) for the L6 models and Supplementary Data **Fig. S4** for the R6 models. The L6_000, L6_0007 and L6_0118 refined structures gave the best fit with the experimental data. Note that the L6_0617 model, which initially had a low packing energy in the grid-search (**Table 1**) exhibited the highest R_1 after refinement (**Table 2**). In addition, although the four selected R6 starting models had low packing energies and R_{ED}-factors lower than those of the L6 models (**Table 1**), the *R*-factors of the refined models (Supplementary Data **Fig. S4**) were both higher than those of the L6 models (**Table 2**). This agrees with previous reports that concluded that the left-handed amylose single helices were favored in V-type complexes [39,63].

Focusing on the four L6 models, several observations can be done. The L6_0000 model is the only one for which the position of some helices significantly changed during the refinement. The alignment along the *a*-axis was broken although the helices are still aligned along *b*, the rows alternatively shifted by ±*b*/8. For L6_0007, this zig-zag organization pre-existed in the starting model and the helices did not significantly move during refinement. In terms of helix position, the models refined from L6_0000 and L6_0007 are indeed similar. In the model refined from L6_0118, the helices are also organized in rows but their position in the unit cell is different (-*b*/4 for the first row), which results in a different distribution of up and down antiparallel helices. In addition, in this

model, due to the position of the $P2_12_12_1$ symmetry axes (Supplementary Data **Fig. S1**), the guest butan-1-ol and water molecules are duplicated in such a way that 2 of the 4 interhelical pockets contains 2 butan-1-ol while the two others contain only water molecules. For the same symmetry reason, the butan-1-ol guests are also grouped in the 2 interhelical spaces of the model refined from L6_0617, the water molecules being distributed in all other interstitial cavities. In this latter model, the amylose helices did not move from their initial position after refinement.

Two out of the four tested L6 models converged towards a similar helix organization with rows parallel to the *b*-axis and shifted by ±*b*/8 with respect to one another. This configuration thus appears to be robust and indeed validates the geometrical model surmised by Helbert and Chanzy [25]. The models refined from L6_0000 or L6_0007 had better agreement with experimental diffraction data, probably due to the higher effective degree of freedom since the guests can move without being trapped in the initial arrangement. In one unit cell, 1 butan-1-ol molecule is located inside each of the 4 helices, and 4 butan-1-ol and 20 water molecules are distributed into the 4 interhelical spaces. Various projections of the model refined from L6_0000 are shown in **Fig. 8** Two types of voids traverse the crystal along the *c*-axis. In conjunction with the experimental data, their dimension and shape contribute to determine the orientation of the butan-1-ol guests. On the one hand, the cavities inside the helices are narrow cylinders and, accordingly, butan-1-ol molecules are aligned along the helical axis (**Fig. 8b**). On the other hand, the interhelical voids are wider and the butan-1-ol guests can adopt various orientations, sharing the space with water molecules. However, after optimization against the ED data, butan-1-ol molecules are oriented nearly perpendicular to the helical axis (**Fig. 8c**).

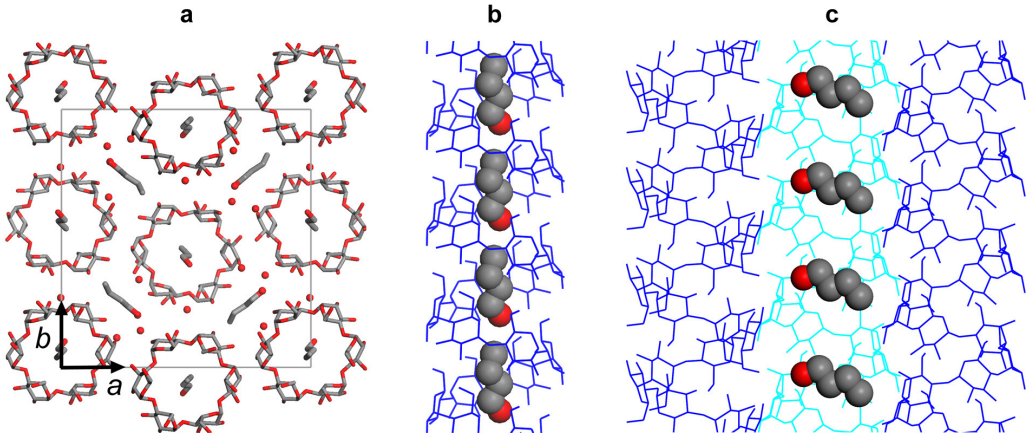

Figure 8. a) Axial view of the $V_{butan\text{-}1\text{-}ol}$ structure refined from the L6_0000 starting model. Butan-1-ol and water molecules are distributed inside the helices and in-between. The hydrogen atoms have been omitted for clarity. b,c) Longitudinal views of the model highlighting the location of butan-1-ol in the intra- and interhelical cavities (b and c, respectively). Several unit cells are displayed. Amylose helices are drawn as a blue wireframe. The water molecules and hydrogen atoms have been omitted for clarity.

Structural parameters that describe the helix conformation in the selected models are given in **Table S4** (**Scheme S1**). The optimized ω angle values in the refined L6_0000 model are all dispersed around the *gg* orientation of the hydroxymethyl groups. In contrast, while the hydroxymethyl groups of only two of the glucose residues in the refined L6_0007 model remain in the *gg* orientation. Interestingly, two of them have ω values close to 0° and their O5 and O6 oxygen atoms are consequently eclipsed. An alternative interpretation of this unusual behavior implies a statistical disorder in the position of these two hydroxymethyl groups adopting the two *gg* and *gt* orientations with partial occupancies. Indeed 0° corresponds to the maximum of the energy barrier that separates the minima at -60° (*gg*) and +60° (*gt*). The model derived from the diffracted data may then correspond to an average structure of the conformation of the amylose chains.

The SHELXL optimization revealed that the L6_0007 model is the most favorable with respect to the electron diffraction data with a R_1 of 0.15 but the L6_0000 model best reproduces the X-ray diffraction with R_{XRD} = 0.16. However, since the C6 carbon signal in the NMR spectrum is broad and centered at 61 ppm, and since there is no peak between 62.5 and 64.5 ppm, the hydroxymethyl groups are thus exclusively dispersed around the *gg* orientation. This aspect is perfectly satisfied by the refined L6_0000 structure but not well reproduced by the L6_0007 one.

Fig. 9a illustrates the good agreement between the experimental and calculated base-plane ED patterns, while **Fig. 9b** compares the observed XRD profile recorded on a mat of hydrated crystals and those simulated from the refined L6_0000 structure. The profile in **Fig. 9b2**, calculated assuming a random crystallite orientation, is a powder profile. However, during the specimen preparation, the settling of the lamellar crystals into the mat promoted a flat-on orientation. Since the experimental profile (**Fig. 9b1)** was recorded with the X-ray beam more or less perpendicular to the film surface (parallel to the *c*-axis), almost no *hkl* ($I \neq 0$) reflections were observed (**Fig. 3b**). Therefore, to be more consistent, we introduced a preferred orientation by modifying the March-Dollase parameter in Mercury, in such a way that the intensity of reflections with orientations close to the [001] *c*-axis was decreased [48]. The simulated profile (**Fig. 9b3**) thus showed a better agreement with the experimental one (**Fig. 9b1**), as expressed as well by a low R_{XRD} factor.

As seen in **Fig. S5**, all the H-bonds correspond to strong and moderate interactions with the O···O distances ranging from 0.22 to 0.33 nm [64]. There are several intramolecular H-bonds, especially those between the O6 with the O1, O5 and O6 of the adjacent glucosyl residue. In addition, some H-bonds occur between glucosyl residues of contiguous helical turns such as O31···O61[x,y,1+z], O63···O23[x,y,1+z], O64···O34[x,y,1+z]. However, there is no evidence for H-bonds between O2 and O3 of each pair of contiguous glucosyl residues which were reported in previous studies for the V_h structure [16,63]. Besides, several intermolecular H-bonds between neighboring helices are also found for $V_{butan\text{-}1\text{-}ol}$ while they are absent in V_h [63]. In addition, water and butan-1-ol molecules located in the interstitial space form H-bonds between themselves and the adjacent single helices. These inter- and intrahelical H-bonds participate to the stability of the orthorhombic packing in the $V_{butan\text{-}1\text{-}ol}$ structure.

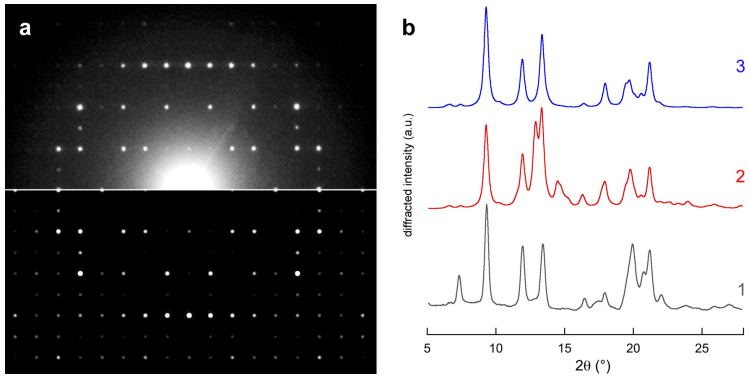

Fig. 9. a) Observed (top) and calculated (bottom) base-plane ED pattern of the $V_{butan\text{-}1\text{-}ol}$ structure refined from the L6_0000 starting model; b1) experimental XRD profile recorded from a hydrated mat of $V_{butan\text{-}1\text{-}ol}$ crystals (beam perpendicular to the mat); b2) powder profile calculated with Mercury [45] (FWHM = 0.37); b3) calculated profile considering a preferred orientation along the *c*-axis (March-Dollase parameter = 3) [48].

By using a standard refinement procedure, we obtained a model that is chemically acceptable and agrees with the diffraction data, under the assumption that all molecules in the unit cell are fixed at a crystallographic position. On the one hand, the final lateral arrangement of the helices is robust and does not depend much on the starting coordinates, with a limited degree of freedom, under the constraint that the helices have to be oriented along the *c*-axis. On the other hand, the position of butan-1-ol and water molecules have a high degree of freedom. We placed the molecules manually, which seems to dictate the trajectory during the refinement. The global best match to the experiment is thus not necessarily reached. In addition, we worked under the hypothesis that the guest molecules also had to follow the crystallographic symmetry and were located at crystallographic positions. It is still not clear to what extent dynamic or static disorder exists in the structure. Since the experimentally available information is limited, further studies require a more extensive use of theoretical energy calculation beyond our current Buckingham's potential.

4. Conclusion

Our approach of structure determination yielded a model for $V_{butan\text{-}1\text{-}ol}$ that agrees with our experimental observations. The helicity and position of the amylose single helices in the unit cell appear to be robust. The final model confirms the hypothesis previously made by Helbert and Chanzy [25]. The unit cell is orthorhombic and contains 4 antiparallel left-handed 6-fold helices. The helices form rows parallel to the *b*-axis alternatively shifted by ±*b*/8 with respect to one another. Since SHELXL refined the models against base-plane ED data, the atomic positions along *c*-axis are less certain than those in the (*a*,*b*) plane. In order to ascertain the 3D model, it will be necessary to enrich the datasets by collecting ED patterns from crystals rotated about selected axes of the reciprocal space, *e.g. a** or *b**, to observe the higher-order *hkl* reflections with $I \neq 0$. Such patterns were indeed collected by Helbert and Chanzy [25] but the intensities were not quantified for structure refinement.

The $V_{butan\text{-}1\text{-}ol}$ crystals belong to the so-called $V6_{II}$ family that also comprises complexes with pentan-1-ol [25], several linear saturated fatty acids [36] and some aliphatic diols [37]. Considering the similarities in diffraction data (albeit minor variations in the intensities), we can assume that the amylose helicity and helix organization are similar for these crystalline complexes, although the stoichiometry and location of the guest ligands and water molecules remain to be elucidated. The structure determined in the present study, and in particular the conformation and distribution of the amylose helices in the unit cell, can thus be used as a template for further calculations on V-type complexes with the same crystal structure but incorporating different guests. Our general approach of combining a packing energy analysis with a structure refinement from diffraction data has proven useful to determine plausible molecular models for $V6_{II}$ and $V7_{II}$ [39] structures. It can certainly be extended to other V-amylose allomorphs that contain 6-, 7- or 8-fold helices.

Acknowledgements

We thank LabEx ARCANE and CBH-EUR-GS (Investissements d'Avenir - grant agreement #ANR-17-EURE-0003) for funding the PhD thesis of C.A.K.L., the NanoBio-ICMG platform (UAR 2607, Grenoble) for granting access to the electron microscopy and NMR facilities, the Glyco@Alps program (Investissements d'Avenir - grant agreement #ANR-15-IDEX-02), and Henri Chanzy for stimulating discussions and his critical reading of the manuscript. CERMAV and DPM are part of Institut Carnot PolyNat (Investissements d'Avenir #ANR-11-CARN-030-01).

References

[1] J. R. Katz, Abhandlungen zur physikalischen Chemie der Stärke und der Brotbereitung. I. Über die Änderungen im Röntgenspektrum der Stärke beim Backen und beim Altbackenwerden des Brotes, Z. Physikal. Chem. 150A (1930) 37–59, https://doi.org/10.1515/zpch-1930-15005.

[2] J. R. Katz, J. C. Derksen, Abhandlungen zur physikalischen Chemie der Stärke und der Brotbereitung. XIV. Ist die Stärke im Stärkekleister kristallinisch oder amorph ? Z. Physikal. Chem. 167A (1933) 129–136, https://doi.org/10.1515/zpch-1933-16714.

[3] R. S. Bear, The significance of the “V” X-ray diffraction patterns of starches, J. Am. Chem. Soc. 64 (1942) 1388–1392, https://doi.org/10.1021/ja01258a043.

[4] K. H. Meyer, P. Bernfeld, E. Wolff, Recherches sur l'amidon III. Fractionnement et purification de l'amylose de maïs naturel, Helw. Chim. Acta 23 (1940) 854–864, https://doi.org/10.1002/hlca.194002301110.

[5] T.J. Schoch, Fractionation of starch by selective precipitation with butanol, J. Am. Chem. Soc. 64 (1942) 2957–2961, https://doi.org/10.1021/ja01264a065.

[6] R. W. Kerr, O. R. Trubell, G. M. Severson, On the multiple amylose concept of starch. II. Amylopectin and amylose. Cereal Chem. 19 (1942) 64–81.

[7] R. W. Kerr, G. M. Severson, On the multiple amylose concept on starch. III. The isolation of an amylose in crystalline form. J. Am. Chem. Soc. 65 (1943) 193–198, https://doi.org/10.1021/ja01242a015.

[8] K. G. Krishnaswamy, A. Sreenivasan, Separation and determination of the amylose and amylopectin fractions of starch, J. Biol. Chem. 176 (1948) 1253–1261.

[9] R. S. Higginbotham, G. A. Morrison, The fractionation of starch. Part II – The separation of amylose and amylopectin, J. Text. Inst. Trans. 40 (1940) T208–T219, https://doi.org/10.1080/19447024908659450.

[10] D. Goodison, R. S. Higginbotham, The fractionation of starch. Part VI – The fractionation of amyloses, J. Text. Inst. Trans. 42 (1951) T249–T273, https://doi.org/10.1080/19447027.1951.10750272.

[11] W. Banks, C. T. Greenwood, The fractionation of laboratory-isolated cereal starches using dimethyl sulphoxide, Die Stärke 12 (1967) 394–398, https://doi.org/10.1002/star.19670191202.

[12] G. K. Adkins, C. T. Greenwood, Studies on starches of high amylose content, Carbohydr. Res. 11 (1969) 217–224, https://doi.org/10.1016/S0008-6215(00)82299-5.

[13] R. E. Rundle, F. C. Edwards, The configuration of starch in the starch-iodine complex. IV. An X-ray diffraction investigation of butanol-precipitated amylose, J. Am. Chem. Soc. 65 (1943) 2200–2203, https://doi.org/10.1021/ja01249a016.

[14] R. M. Valetta, F. J. Germino, R. E. Lang, R. J. Moshy, Amylose “V” complexes: Low molecular weight primary alcohols, J. Polym. Sci. A 2 (1964) 1085–1094, https://doi.org/10.1002/pol.1964.100020306.

[15] M. E. Hinkle, H. F. Zobel, X-ray diffraction of oriented amylose fibers. III. The structure of amylose-n-butanol complexes, Biopolymers 6 (1968) 1119–1128, https://doi.org/10.1002/bip.1968.360060807.

[16] G. Rappenecker, P. Zugenmaier, Detailed refinement of the crystal structure of Vh-amylose, Carbohydr. Res. 89 (1981) 11–19, https://doi.org/10.1016/S0008-6215(00)85225-8.

[17] V. G. Murphy, B. Zaslow, A. D. French, The structure of V amylose dehydrate: A combined X-ray and stereochemical approach, Biopolymers 14 (1975) 1487–1501, https://doi.org/10.1002/bip.1975.360140714.

[18] N. Hirai, T. Yasui, S. Fujita, Y. Yamashita, Physicochemical study on crystalline texture of starch. I. Single crystals of α-amylose, Kobunshi Kagaku 196 (1963) 413–416.

[19] Y. Yamashita, Physicochemical study on crystalline texture of starch. II. The fold structure of amylose helices in single crystals, Kobunshi Kagaku (1964) 103–108.

[20] R. St. J. Manley, Chain folding in amylose crystals, J. Polym. Sci. A 2 (1964) 4503–4515, https://doi.org/10.1002/pol.1964.100021019.

[21] H. Bittiger, E. Husemann, Elektronenmikroskopische Untersuchungen an Kristallen von Amylosekomplexen und Polyäthylen, Kolloid Z. Z. Polym. 232 (1969) 661–668, https://doi.org/10.1007/BF01500161.

[22] Y. Yamashita, Single crystals of amylose V complexes, J. Polym. Sci. A 3 (1965) 3251–3260, https://doi.org/10.1002/pol.1965.100030919.

[23] Y.-H. Yamashita, J. Ryugo, K. Monobe, An electron microscopic study on crystals of amylose V complexes, J. Electron Microsc. 22 (1973) 19–26, https://doi.org/10.1093/oxfordjournals.jmicro.a049858.

[24] F. P. Booy, H. Chanzy, A. Sarko, Electron diffraction study of single crystals of amylose complexed with n-butanol, Biopolymers 18 (1979) 2261–2266, https://doi.org/10.1002/bip.1979.360180913.

[25] W. Helbert, H. Chanzy, Single crystals of V-amylose complexed with n-butanol or n-pentanol: structural features and properties. Int. J. Biol. Macromol. 16 (1994) 207–213, https://doi.org/10.1016/0141-8130(94)90052-3.

[26] T. J. Schoch, The fractionation of starch, Adv. Carbohydr. Chem. 1 (1945) 247–277, https://doi.org/10.1016/s0096-5332(08)60411-7.

[27] J. Muetgeert, The fractionation of starch, Adv. Carbohydr. Chem. 16 (1962) 299–333, https://doi.org/10.1016/S0096-5332(08)60265-9.

[28] Y. Takeda, S. Hizukuri, B. O. Juliano, Purification and structure of amylose from rice starch, Carbohydr. Res. 148 (1986) 299–308, https://doi.org/10.1016/s0096-5332(08)60411-7.

[29] J. D. Klucinec, D. B. Thompson, Fractionation of high-amylose maize starches by differential alcohol precipitation and chromatography of the fractions, Cereal Chem. 75 (1998) 887–896, http://dx.doi.org/10.1094/CCHEM.1998.75.6.887.

[30] H. J. Cornell, S.J. McGrane, C. J. Rix, A novel and rapid method for the partial fractionation of starch using 1-butanol in the presence of thiocyanate, Starch/Stärke 51 (1999) 335–341.

[31] V. Corcuera, E. M. Salmoral, J. C. Salerno, C. R. Krisman, Starch molecular fractionation of bread wheat varieties, Agriscientia 24 (2007) 11–18.

[32] X. Hu, C. Liu, Z. Jin, Y. Tian, Fractionation of starch hydrolysate into dextrin fractions with low dispersity by gradient alcohol precipitation, Sep. Purif. Technol. 151 (2015) 201–210, https://doi.org/10.1016/j.seppur.2015.07.044.

[33] M. Ulbrich, M. L. Salazar, E. Flöter, Separation and molecular characterization of the amylose- and amylopectin-fraction from native and partially hydrolyzed potato starch, Starch/Stärke 69 (2017) 1600228, https://doi.org/10.1002/star.201600228.

[34] A. F. Doblado-Maldonado, S. V. Gomand, B. Goderis, J. A. Delcour, Methodologies for producing amylose: A review, Crit. Rev. Food Sci. Nutr. 57 (2017) 407–417, https://doi.org/10.1080/10408398.2014.954030.

[35] W. Dvonch, H. J. Yearlian, R. L. Whistler, Behavior of low molecular weight amylose with complexing agents, J. Am. Chem. Soc. 72 (1950) 1748–1750, https://doi.org/10.1021/ja01160a094.

[36] C. A. K. Le, L. Choisnard, D. Wouessidjewe, J.-L. Putaux, Polymorphism of crystalline complexes of V-amylose with fatty acids, Int. J. Biol. Macromol. 119 (2018) 555–564, https://doi.org/10.1016/j.ijbiomac.2018.07.163.

[37] C. A. K. Le, L. Choisnard, D. Wouessidjewe, J.-L. Putaux, Polymorphism of V-amylose complexed with aliphatic diols, Polymer 213 (2021) 123302, https://doi.org/10.1016/j.polymer.2020.123302.

[38] J. Laugier, B. Bochu, LMGP-Suite: Suite of programs for the interpretation of X-ray experiments, 2004, http://www.cristal.org/DU-SDPD/nexus/ccp14/web/tutorial/lmgp/.

[39] Y. Nishiyama, K. Mazeau, M. Morin, M. B. Cardoso, H. Chanzy, J.-L. Putaux, Molecular and crystal structure of 7-fold V-amylose complexed with 2-propanol. Macromolecules 43 (2010) 8628–8636, https://doi.org/10.1021/ma101794w.

[40] A. K. Rappé, C. J. Casewit, K. Colwell, W. A. Goddard III, W. M. Skiff, UFF, a full periodic table force field for molecular mechanics and molecular dynamics simulations, J. Am. Chem. Soc. 114 (1992) 10024–10035, https://doi.org/10.1021/ja00051a040.

[41] Materials Studio 5.5. Accelrys Inc., San Diego, CA, https://www.3dsbiovia.com/portfolio/materials-studio.html.

[42] M. Dauchez, P. Derreumaux, G. Vergoten, Vibrational molecular force field of model compounds with biologic interest. II. Harmonic dynamics of both anomers of glucose in the crystalline state, J. Comput. Chem. 14 (1993) 263–277, https://doi.org/10.1002/jcc.540140303.

[43] Computational Crystallography Toolbox, https://cctbx.github.io/.

[44] Gnuplot 5.2, http://gnuplot.info.

[45] C. F. Macrae, I. J. Bruno, J. A. Chisholm, P. R. Edgington, P. McCabe, E. Pidcock, L. Rodriguez-Monge, R. Taylor, J. van de Streek, P. A. Wood, Mercury CSD 2.0 - new features for the visualization and investigation of crystal structures, J. Appl. Cryst. 41 (2008) 466–470, https://doi.org/10.1107/S0021889807067908.

[46] G. M. Sheldrick, Crystal structure refinement with SHELXL, Acta Crystal. C: Struct. Chem. 71 (2005) 3–8, https://doi.org/10.1107/S2053229614024218.

[47] J. M. Cowley, L. M. Peng, G. Ren, S. L. Dudarev, M.J. Whelan, International Tables for Crystallography. Volume C: Mathematical, Physical and Chemical Tables (Eds: E. Prince, A. J. C. Wilson), Kluwer Academic Publishers, 2004, p 282.

[48] W. A. Dollase, Correction of intensities for preferred orientation in powder diffractometry: Application of the March model, J. Appl. Cryst. 19 (1986) 267–272, https://doi.org/10.1107/S0021889886089458.

[49] P. Le Bail, C. Rondeau, A. Buléon, Structural investigation of amylose complexes with small ligands: helical conformation, crystalline structure and thermostability, Int. J. Biol. Macromol. 35 (2005) 1–7, https://doi.org/10.1016/j.ijbiomac.2004.09.001.

[50] J.D.H. Donnay, Rules for the conventional orientation of crystals, Am. Mineral. 28 (1943) 313–328.

[51] F. Horii, H. Yamamoto, A. Hirai, R. Kitamaru, Structural study of amylose polymorphs by cross-polarization-magic-angle spinning, 13C-N.M.R. spectroscopy, Carbohydr. Res. 160 (1987) 29–40, https://doi.org/10.1016/0008-6215(87)80301-4.

[52] R. P. Veregin, C. A. Fyfe, R. H. Marchessault, Investigation of the crystalline “V” amylose complexes by high-resolution ^{13}C CP/MAS NMR spectroscopy, Macromolecules 20 (1987) 3007–3012, https://doi.org/10.1021/ma00178a010.

[53] J. Kawada, R. H. Marchessault, Solid state NMR and X-ray studies on amylose complexes with small organic molecules, Starch/Stärke 56 (2004) 13–19, https://doi.org/10.1002/star.200300222.

[54] I. C. Jones, G. J. Sharman, J. Pidgeon, ^{1}H and ^{13}C NMR data to aid the identification and quantification of residual solvents by NMR spectroscopy, Magn. Res. Chem. 43 (2005) 497–509, https://doi.org/10.1002/mrc.1578.

[55] M. J. Gidley, S. M. Bociek, ^{13}C CP/MAS NMR studies of amylose inclusion complexes, cyclodextrins, and the amorphous phase of starch granules: Relationships between glycosidic linkage conformation and solid-state ^{13}C chemical shifts, J. Am. Chem. Soc. 110 (1988) 3820–3829. https://doi.org/10.1021/ja00220a016.

[56] J.-L. Putaux, M. B. Cardoso, M. Morin, Y. Hu, D. Dupeyre, Single crystals of V-amylose inclusion complexes, Macromol. Symp. 273(1) (2008) 1–8. https://doi.org/10.1002/masy.200851301.

[57] C. Rondeau-Mouro, P. Le Bail, A. Buléon, Structural investigation of amylose complexes with small ligands: inter- or intra-helical associations?, Int. J. Biol. Macromol. 34 (2004) 251–257, https://doi.org/10.1016/j.ijbiomac.2004.09.002.

[58] C. A. K. Le, Y. Ogawa, F. Dubreuil, F. Grimaud, K. Mazeau, G. R. Ziegler, S. Tanwar, Y. Nishiyama, G. Potocki-Veronese, L. Choisnard, D. Wouessidjewe, J.-L. Putaux, Crystal and molecular structure of V-amylose complexed with ibuprofen, Carbohydr. Polym. 261 (2021) 117885, https://doi.org/10.1016/j.carbpol.2021.117885.

[59] F. Horii, A. Hirai, R. Kitamaru, Solid-state ^{13}C-NMR study of conformations of oligosaccharides and cellulose conformation of CH_2OH group about the exo-cyclic C-C bond, Polymer Bulletin 10 (1983) 357–341, https://doi.org/10.1007/BF00281948.

[60] R. P. Veregin, C. A. Fyfe, R. H. Marchessault, M. G. Taylor, Correlation of ^{13}C chemical shifts with torsional angles from high-resolution, ^{13}C-C.P.-M.A.S. N.M.R. studies of crystalline cyclomalto-oligosaccharide complexes, and their relation to the structures of the starch polymorphs, Carbohydr. Res. 160 (1987) 41–56, https://doi.org/10.1016/0008-6215(87)80302-6.

[61] P. Derollez, A. Hédoux, Y. Guinet, F. Danède, L. Paccou, Structure determination of the crystalline phase of n-butanol by powder X-ray diffraction and study of intermolecular associations by Raman spectroscopy, Acta Cryst. B69 (2013) 195–202, https://doi.org/10.1107/S2052519213004843.

[62] I. Doroshenko, Y. Vaskivskyi, Y. Chernolevska, Structural transformations in solid and liquid n-butanol from FTIR spectroscopy, Mol. Cryst. Liq. Cryst. 697 (2020) 11–19, https://doi.org/10.1080/15421406.2020.1731098.

[63] J. Brisson, H. Chanzy, W.T. Winter, The crystal and molecular structure of V_H amylose by electron diffraction analysis. Int. J. Biol. Macromol. 13 (1991) 31–39, https://doi.org/10.1016/0141-8130(91)90007-H.

[64] G. A. Jeffrey, An Introduction to Hydrogen Bonding, New York: Oxford University Press, 1997, p 303.

Supplementary Data

Table S1. Observed and calculated X-ray diffraction angles (2θ) of $V_{butan\text{-}1\text{-}ol}$ crystals, indexed on the basis of an orthorhombic unit cell with *a* = 2.655 nm, *b* = 2.708 nm and *c* = 0.798 nm.

h k l	$2\theta_{obs}$ (°)	$2\theta_{cal}$ (°)
1 2 0	7.34	7.33
2 2 0	9.34	9.33
3 2 0	11.95	11.95
1 4 0	13.49	13.50
3 4 0	16.49	16.49
1 4 1	17.50	17.50
5 2 0	17.95	17.94
2 6 0	20.80	20.79
5 4 0	21.25	21.26
3 6 0	22.10	22.11
4 6 0	23.84	23.84
5 6 0	25.91	25.91
8 1 0	27.07	27.07

Table S2. List of observed reflections and their intensities (I_{obs}) in the base-plane electron diffraction pattern (l = 0) of $V_{butan\text{-}1\text{-}ol}$ crystals. σ is the standard error.

h	*k*	I_{obs}	σ
1	1	0.00	0.00
0	2	30.95	0.46
2	0	33.49	0.32
1	2	7.76	1.50
2	1	0.00	0.00
2	2	242.34	0.18
1	3	0.00	0.00
3	1	0.00	0.00
2	3	0.00	0.00
3	2	254.15	0.20
0	4	0.00	0.00
1	4	163.88	0.12
4	0	186.04	0.13
4	1	0.00	0.00
3	3	0.00	0.00
2	4	0.00	0.00
4	2	1.98	0.46
3	4	140.35	0.13
1	5	3.15	0.45
4	3	2.14	0.68
5	1	0.00	0.00
2	5	0.00	0.00
5	2	254.51	0.15
4	4	11.92	0.18
3	5	2.78	0.41
5	3	55.99	0.11
0	6	509.27	0.17
1	6	279.37	0.13
2	6	292.87	0.12
4	5	3.60	0.32
5	4	527.36	0.17
3	6	102.05	0.10
1	7	3.04	0.30
5	5	6.58	0.21
4	6	10.41	0.17
3	7	0.00	0.00
5	6	27.54	0.10
0	8	0.00	0.00
1	8	0.00	0.00
4	7	2.03	0.32
2	8	13.62	0.15
3	8	3.19	0.32
5	7	0.00	0.00
4	8	3.71	0.20
5	8	0.00	0.00
6	0	433.05	0.15
6	1	22.05	0.12
6	2	265.98	0.16
6	3	2.91	0.46
6	4	7.04	0.17
6	5	3.79	0.27
6	6	5.83	0.19
6	7	0.90	0.57
6	8	7.28	0.14
7	1	0.00	0.00
7	2	0.00	0.00
7	3	0.00	0.00
7	4	6.01	0.19
7	5	0.00	0.00
7	6	1.35	0.31
7	7	2.15	0.28
7	8	0.00	0.00
8	0	30.08	0.10
8	1	0.00	0.00
8	2	0.00	0.00
8	3	0.00	0.00
8	4	1.55	0.29
8	5	0.00	0.00
8	6	5.50	0.15
8	7	0.00	0.00
8	8	1.96	0.29

Table S3. Helix position, packing energy, R_{ED}-factor and R_{XRD}-factor of selected models based on left- and right-handed 7-fold amylose single helices (L7 and R7), within 1/16th of the unit cell (see color maps in **Fig. S2**). The selected models correspond to a local minimum in either one of the three maps.

Model name	Position of the helix center (fractional coordinates)		Packing energy (kJ/glucosyl unit)	R_{ED}-factor	R_{XRD}-factor
	x	y			
L7_0008	0.00	0.08	1347.5	0.57	0.46
L7_0016	0.00	0.16	1423.9	0.57	0.53
L7_0019	0.00	0.19	2610.9	0.60	0.39
L7_0315	0.03	0.15	170.1	0.69	0.62
L7_1923	0.19	0.23	3898.3	0.68	0.41
R7_0008	0.00	0.08	1873.4	0.53	0.47
R7_0016	0.00	0.16	1443.5	0.53	0.54
R7_0219	0.02	0.19	1861.3	0.59	0.40
R7_0314	0.03	0.14	357.2	0.68	0.66
R7_1923	0.19	0.23	5008.2	0.67	0.42

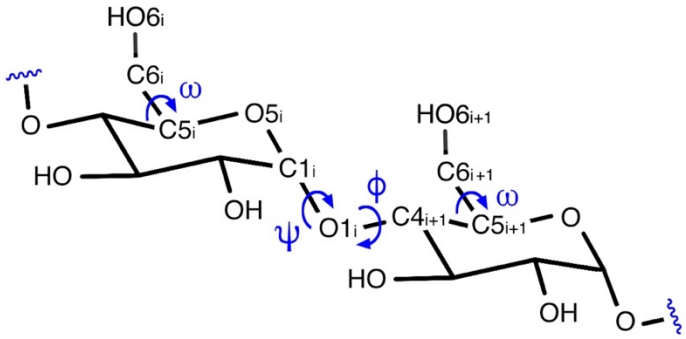

Scheme S1. Atom numbering in two contiguous glucosyl residues of the amylose chain. The ϕ and ψ torsion angles across the glycosidic bond define the relative orientation of the glucosyls. ϕ is defined by the atom sequence $O5_i$-$C1_i$-$O1_i$-$C4_{i+1}$, and ψ by $C1_i$-$O1_i$-$C4_{i+1}$-$C5_{i+1}$. The torsion ω defines the orientation of the hydroxymethyl pendant group on the pyran rings and is defined by the atom sequence $O5_i$-$C5_i$-$C6_i$-$O6_i$, and is -60, 60 and 180° for *gg*, *gt* and *tg,* respectively.

Table S4. Torsion angles describing the conformation of the amylose helix in the $V_{butan\text{-}1\text{-}ol}$ structures refined from the L6_0000 and L6_0007 models. The bond angle τ is defined by (C1-O1-C4). Excluding the orientation of the hydroxymethyl groups which shows singularities in refined model L6_0007, the conformations of the helices are classical and similar from one model to another. Pyran rings are all around the $^4C_1$ shape, as suggested by the intra-residue O1-O4 distances in the range 0.41–0.45 nm and the Φ and Ψ torsion angles are within the accessible angular domains predicted for maltose [A.D. French, Carbohydr. Res. 188 (1989) 206–211, https://10.1016/0008-6215(89)84072-8].

Residue number	Refined L6_0000					Refined L6_0007				
	ϕ (°)	ψ (°)	τ (°)	ω (°)	O1-O4 (nm)	ϕ (°)	ψ (°)	τ (°)	ω (°)	O1-O4 (nm)
1	110.1	-141.1	116.5	-109.7	4.3	116.5	-148.8	116.6	141.7	4.3
2	73.6	-97.9	117.5	-56.9	4.5	81.1	-121.7	117.1	-44.6	4.5
3	113.1	-128.0	118.9	-52.4	4.5	81.2	-110.6	120.3	-91.8	4.5
4	95.9	-143.3	117.3	-101.2	4.2	98.9	-131.1	120.1	1.4	4.4
5	80.0	-104.4	116.6	-99.7	4.4	96.8	-96.3	116.6	82.1	4.4
6	100.4	-127.6	117.0	-49.7	4.4	109.9	-137.3	117.2	-7.0	4.3

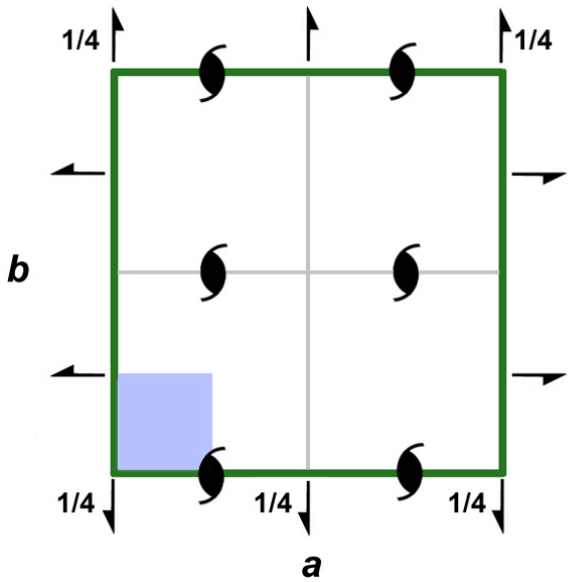

Figure S1. Symmetry of the $P2_12_12_1$ space group. The blue rectangle indicates the 1/16th region in which the packing energy and R_{XRD}- and R_{ED}-factor color maps are displayed in **Figs. 6** and **S2**.

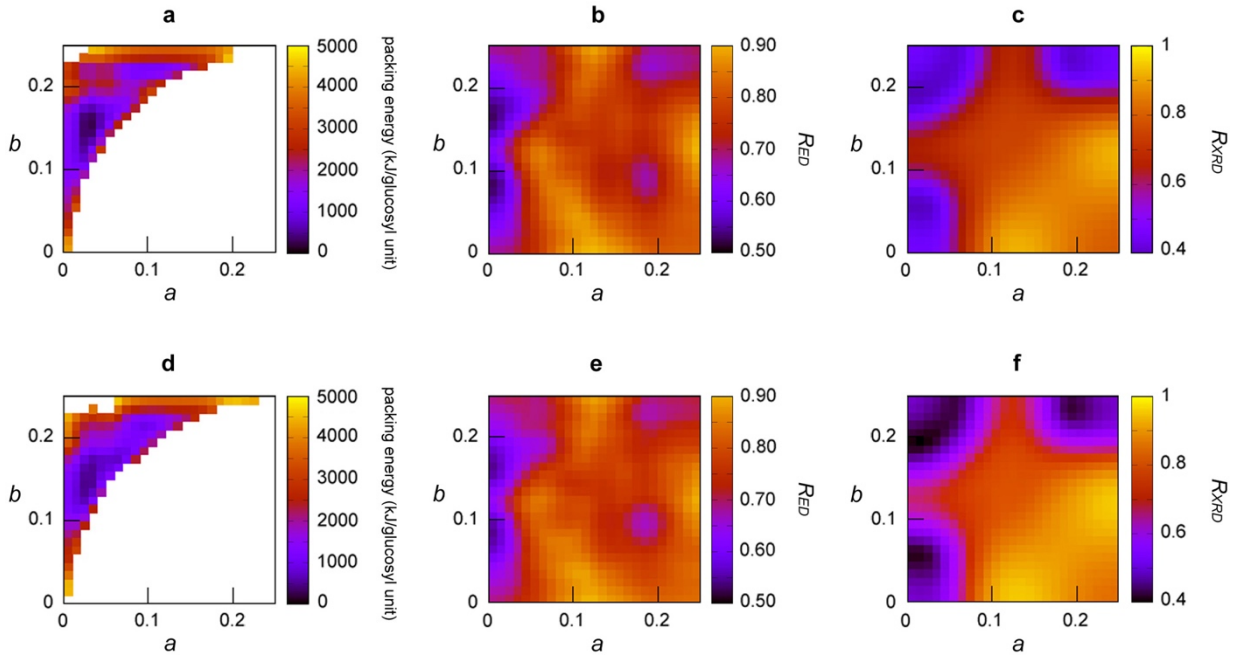

Figure S2. a,d) Color maps of the packing energy of models based on left- (a) and right-handed (b) 7-fold amylose helices (L7 and R7, respectively) without O6H hydroxy groups. The helices were systematically translated and rotated within 1/16th of the (*a,b*) plane of the unit cell; b,e) R_{ED}-factor between the observed and calculated ED diagrams for L7 (b) and R7 (e) helices; c,f) R_{XRD}-factor between the observed and calculated XRD profiles for L7 (c) and R7 (f) helices. The helix position is indicated with fractional coordinates. Considering the symmetry of the $P2_12_12_1$ space group, only 1/16th of the *(a,b)* plane was displayed ($0 \leq x \leq 0.24$, $0 \leq y \leq 0.24$). In all maps, the minima are indicated by arrows. Both *R*-factors were calculated using **Eq. 1**.

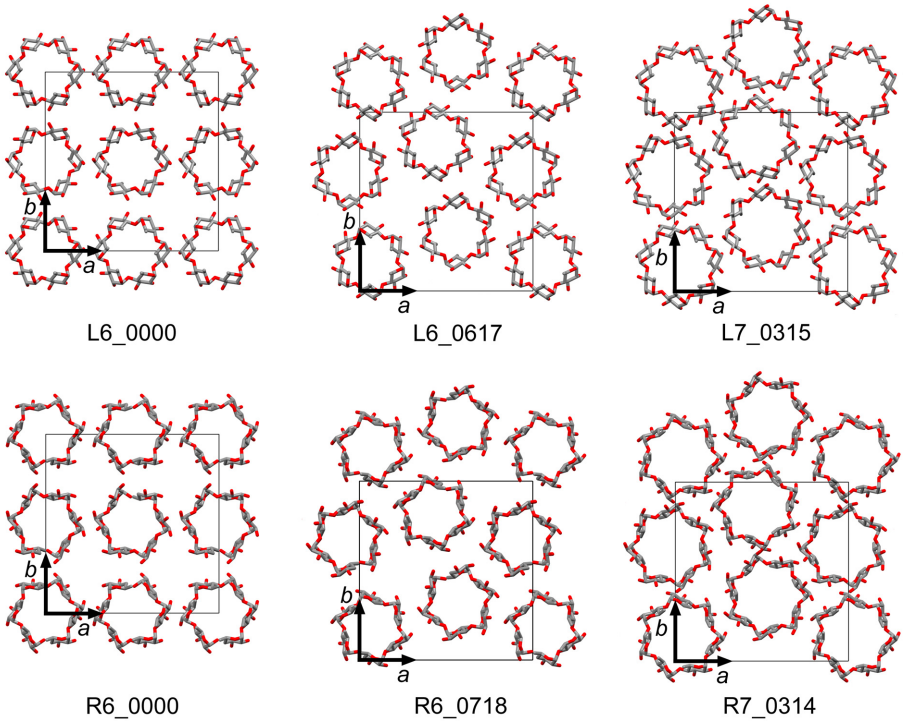

Figure S3. Projection on the *(a,b)* plane of L6, R6, L7 and R7 models corresponding to minima in packing energy maps. The helices are stereoregular and without O6H hydroxy groups. The hydrogen atoms have not been drawn for clarity.

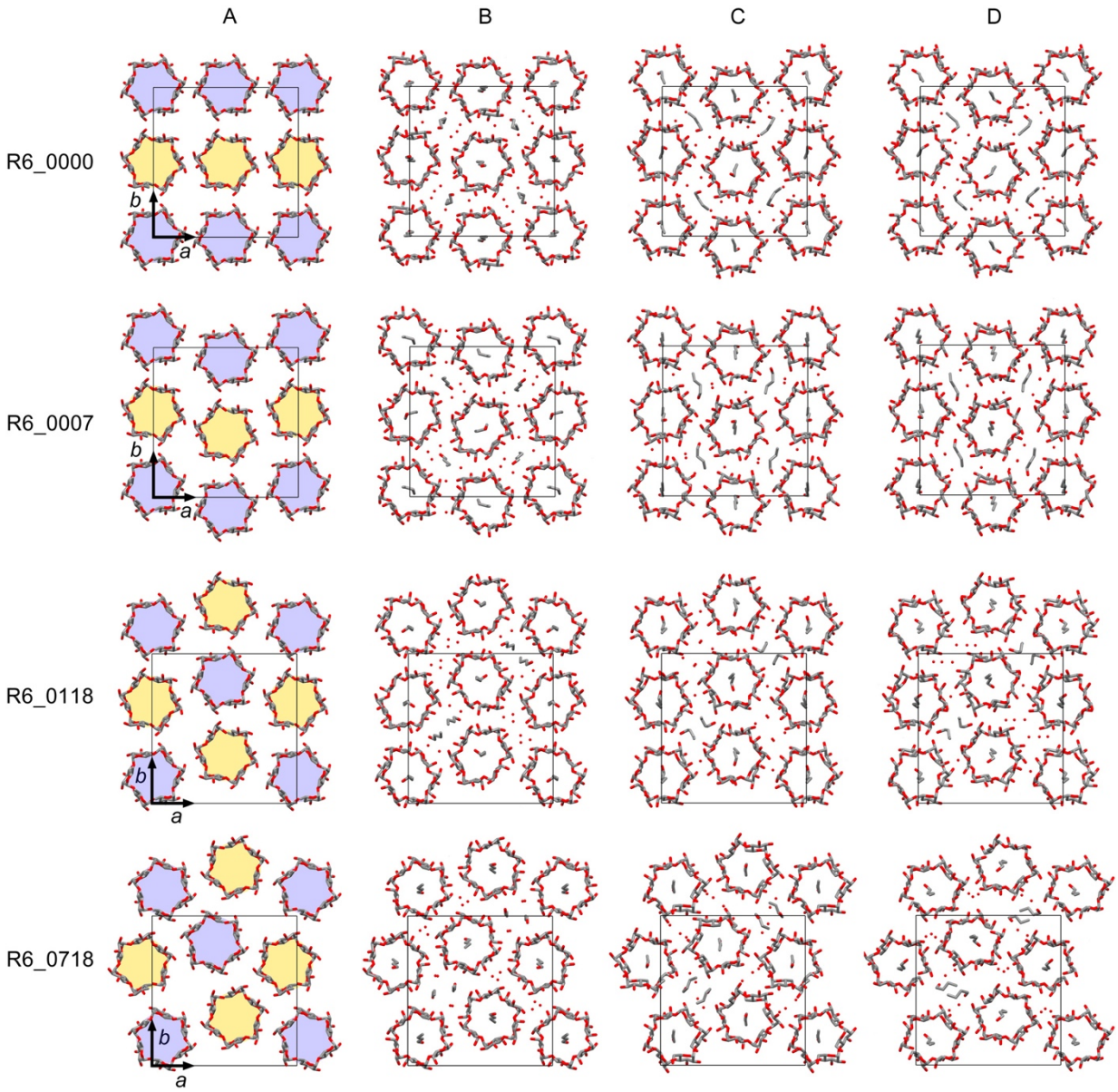

Figure S4. Column A: projections on the *(a,b)* plane of the R6 models corresponding to minima in the maps of **Fig. S2** (**Table 1**). The helices are stereoregular and without O6H hydroxy groups. The blue and yellow colors distinguish between up and down helices organized in an antiparallel fashion. Column B: Hydroxymethyl groups in *gg* conformation were added as well as butan-1-ol (*trans* conformation) and water molecules. The models were minimized in Materials Studio then used as input files in SHELXL. Column C: models refined against ED data in SHELXL with the hydroxymethyl conformation constrained to *gg* and butan-1-ol in *trans* conformation; column D: refined models with unrestrained hydroxymethyl conformation. In all models, the hydrogen atoms have been omitted for clarity and the unit cells are indicated.

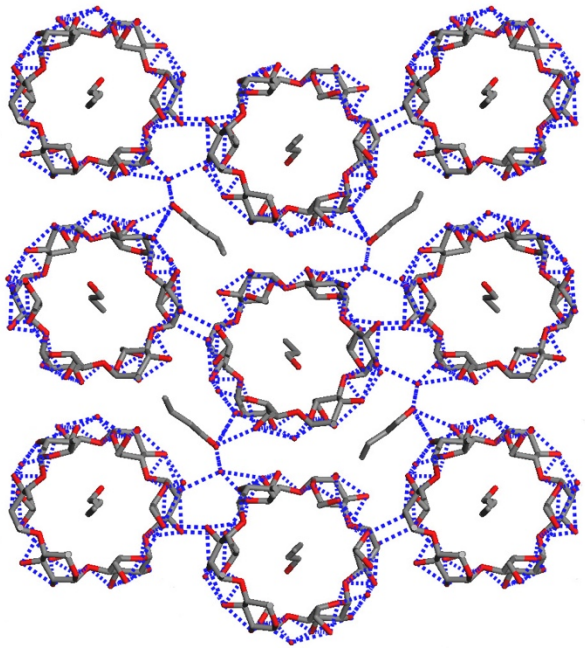

Figure S5. Intra- and intermolecular hydrogen bonds (dotted blue lines) in the model refined from L6_0000, with an O···O distance smaller than 0.33 nm. Hydrogen atoms have been omitted for clarity.